ADVANCED ELECTRONIC MATERIALS Open Access
www.advelectronicmat.de

Check for updates

Hysteresis and Photoconductivity of Few-Layer $ReSe_2$ Field Effect Transistors Enhanced by Air Pressure

*Kimberly Intonti, Enver Faella, Loredana Viscardi, Arun Kumar, Ofelia Durante, Filippo Giubileo, Maurizio Passacantando, Hoi Tung Lam, Konstantinos Anastasiou, Monica F. Craciun, Saverio Russo, and Antonio Di Bartolomeo**

This study reports the optoelectronic characterization of few-layer $ReSe_2$field effect transistors at different pressures. The output curves reveal dominant n-type behavior and a low Schottky barrier at the metal contacts. The transfer curves show a significant hysteresis that can be exploited in memory devices with an order ofmagnitude memory window and good cycling. The devices are dramatically affected by air pressure; their conductance and mobility increase with the lowering pressure that desorbs electronegative air molecules from the surface of the material. The photoresponse under white super-continuum laser illumination reveals that the device exhibits positive photoconductivity (PPC) at ambient and low (≈1 mbar) pressure and negative photoconductivity (NPC) in a higher vacuum (≈10^{-4} mbar). The transition from PPC to NPC can be explained by considering that the photoresponse is affected by molecule desorption, which yields PPC at higher pressure, and defect trapping of photogenerated carriers, which can dominate at lower pressures. The transient behavior of the device exposed to laser pulses shows a faster response and a higher photodetection efficiency at ambient pressure, with the highest signal-to-noise ratio at the valley of the transfer curve between p- and n-type conduction.

1. Introduction

Over the past decade, 2D transition metal dichalcogenides (TMDs) have attracted great attention because of their unique electronic, optical, and mechanical properties.[1–5] Their 2D layered structure, together with their tunable bandgap, is underpinning significant advances in field effect transistors (FETs).[6–8] Group VI atom-based TMDs, including MoS_2, which is the most widely studied material, were also implemented in back-gated transistors used for photodetection, due to their pronounced light-matter interaction, large light absorbance, and efficient photocarrier generation. Extraordinarily large values of photoresponsivity as well as low dark currents have been reported in photodetectors based on these materials.[9–11] However, owing to their high in-plane symmetry, they show an isotropic in-plane response independent of light polarization. Crystals with reduced symmetry, instead, are promising for novel optoelectronic devices, such as those used for augmented reality, health care, and defense technologies, where their anisotropy in the current flow or light polarization is exploited.[12] To date only few 2D materials with strong in-plane anisotropic properties, such as black phosphorus, have been studied, holding back the development of innovative sensing and imaging applications.[13]

Rhenium diselenide ($ReSe_2$), one of the recently discovered group VII TMD materials, is a layered indirect gap semiconductor with several unusual features.[14,15] The crystal growth of ReX_2 (with X = Se or S) is challenging because Re has one of the highest melting points of all metals, whereas S and Se have relatively low melting points and high vapor pressures.[16] Unlike the common hexagonal or octahedral structures seen in most TMDs, $ReSe_2$ crystallizes in a distorted 1T' structure with a triclinic symmetry $P\bar{1}$ which determines highly anisotropic properties. The d^3 electron configuration in the outermost shell of Re is the cause of the displacement of the metal atoms from their octahedral position at the center of the anion cage. As a result of the Peierls distortion, the Re atoms dimerize to form diamond-shaped zigzag Re-Re chains.[16,17]

Contrary to many other 2D TMDs, $ReSe_2$ does not exhibit an indirect to direct band gap transition upon reducing the

K. Intonti, E. Faella, L. Viscardi, A. Kumar, O. Durante, A. Di Bartolomeo
Department of Physics "E.R. Caianiello"
University of Salerno
via Giovanni Paolo II 132, Fisciano84084, Salerno, Italy
E-mail: adibartolomeo@unisa.it

F. Giubileo
CNR-SPIN
via Giovanni Paolo II 132, Fisciano84084, Salerno, Italy

M. Passacantando
Department of Physical and Chemical Science
University of L'Aquila
via Vetoio, Coppito67100, L'Aquila, Italy

H. T. Lam, K. Anastasiou, M. F. Craciun, S. Russo
University of Exeter
Stocker road 6, Exeter, Devon EX4 4QL, UK

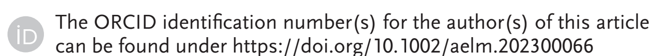
The ORCID identification number(s) for the author(s) of this article can be found under https://doi.org/10.1002/aelm.202300066

© 2023 The Authors. Advanced Electronic Materials published by Wiley-VCH GmbH. This is an open access article under the terms of the Creative Commons Attribution License, which permits use, distribution and reproduction in any medium, provided the original work is properly cited.

DOI: 10.1002/aelm.202300066

number of layers to a single atomic sheet. In addition, the optical and vibrational properties of this 2D system are very weakly dependent on the number of layers. The Raman spectra of the Re-based dichalcogenides are feature-rich, with roughly 18 first–order Raman active modes in the range of 100–300 cm^{-1} that are nondegenerate due to their low symmetry structure, in contrast to other members of TMDs such as MoX_2 and WX_2.[16,18,19]

Earlier studies have shown the use of $ReSe_2$ in a variety of electronic and optoelectronic devices.[20–22] These reports claimed that the absence of a halogen vapor transport route during the growth process results in the n-type doping of the crystal.[16] Low electron mobility (≈2 cm^2 V^{-1} s^{-1}) was found in few-layer $ReSe_2$ FETs at room temperature.[20] A significant increase of the field effect mobility (≈400 cm^2 V^{-1} s^{-1}) as well as a reduction of the hysteresis of the transfer curves were reported in multi-layer samples as a result of reduced Coulomb scattering from surficial adsorbates.[23]

The ambipolar behavior of $ReSe_2$ transistors is also remarkable with on/off current ratios of ≈10^7 for electrons and 10^6 for holes, even with poor subthreshold swings of 3.5 V $decade^{-1}$. $ReSe_2$ is one of the few materials to exhibit ambipolarity in the absence of ionic liquid gating or dielectric, heterostructures, or contact engineering, thus displaying potential for applications in complementary logic electronic devices as inverters, as fabricated and studied by Kang et al.[24] and Lee et al.[25]

Electrical measurements both in the dark and under laser illumination were performed by Jo et al.[26] on back-gated FETs with two different metal contacts (Ti and Pt). They saw that a reduction in the incident laser power induced an exponential increase in photoresponsivity. Indeed, under low power conditions, the scattering phenomenon among the photocarriers was inhibited. The temporal response of the photocurrent at the rising and decreasing edges showed a relatively slow time response of 5.20/5.30 s.

Enhanced photoresponse was reported by Khan et al.,[27] who fabricated few-layer $ReSe_2$ FETs with Sc/Au contacts on an h-BN substrate. They showed a photoresponsivity 100 times higher than other recent $ReSe_2$ photodetectors and attributed it to reduced Schottky barrier heights between metal and $ReSe_2$ and reduced charge scattering of h-BN. A high-performance $ReSe_2$ near-infrared photodetector with high photoresponsivity, a wide detection range, and fast photoswitching time was obtained by an organic molecule-based n-doping technique based on a (3-aminopropyl)trimethoxysilane(APTMS) by Ali et al.[28]

Additionally, monolayer rhenium diselenide exhibited nonvolatile resistive switching behavior in resistive random-access memory (RRAM) devices with sub-nanometer active layer thickness, as demonstrated by Huang et al.[29] They reported a stable multiple-step RESET by applying different levels of DC electrical bias. RRAM devices got increasing interest for the simplicity of their structure, low power consumption, and applicability to neuromorphic computing.

Also, investigating the gas–sensing properties of $ReSe_2$ gave successful results. Nazari et al.[30] fabricated Gr/$ReSe_2$ heterostructures with excellent mobility of 380 cm^2 V^{-1} s^{-1} and high photoresponsivity, detectivity, external quantum efficiency, as well as rapid photoresponse. This remarkable performance was due to the combined result of strong light absorption by $ReSe_2$ and high carrier transport by graphene. The heterostructure was exposed to NO_2 gas under various humidity conditions, returning high response, good reversibility, and gas selectivity under light irradiation of 532 nm.

The novelty of this study is the extensive investigation of the electrical and opto-electronic properties of a few-layer $ReSe_2$ FET in different pressure conditions, from atmospheric pressure to high vacuum. Transfer and output curves are first measured in the dark at atmospheric pressure and room temperature, revealing the n-type conduction of the material, the presence of a low Schottky barrier, and a wide hysteresis that is exploited for memory purposes. We show that the device's properties are dramatically affected by the air pressure. The $ReSe_2$ conductance increases at lower pressures when electronegative molecules are desorbed from the $ReSe_2$ surface. The photoresponse of the device illuminated by a super-continuum white laser is investigated at three different pressures. A positive photoconductivity is observed both at ambient pressure and in low vacuum, enhanced by the photo-assisted desorption of adsorbates. Vice versa, negative photoconductivity is observed in higher vacuum due to the photogating effect of photogenerated charges trapped in defect-induced trap states. Finally, the maximum photocurrent and its transient behavior are estimated by exposing the device to laser pulses.

2. Results and Discussion

2.1. Structural Characterization

Figure 1a shows a schematic representation of the crystal structure of $ReSe_2$ along the a,b and c axes, highlighting the distorted 1T' phase and the diamond shaped Re-Re chains along the in-plane b axis. The thickness of the flake, measured by an atomic force microscope (AFM), reveals that it is 2.8 nm (see Figure 1b), corresponding to four layers as the single layer is 0.65-0.7 nm thick.

The atomic vibrational spectrum, reported in Figure 1c, was recorded using a laser wavelength of 785 nm. The Raman modes occur in the frequency range from 100 to 300 cm^{-1} and are densely placed, except for a gap ≈140 cm^{-1}. Since $ReSe_2$ has 12 atoms per unit cell, 36 normal modes are expected. Given the unit cell point group symmetry C_i indicating that it has no symmetry except a center of inversion and since all atoms are displaced from the inversion center, all normal modes are nondegenerate: there are 18 Raman-active A_g modes, 15 infrared active A_u modes and 3 zero-frequency A_u modes.[18] However, usually not all the peaks are resolved because they overlap substantially, making it difficult to fit the spectra to locate all 18 Raman active modes. Despite this, the comparison between the obtained spectrum and others reported in the literature confirms that the flake material is $ReSe_2$, as demonstrated by the in-plane E_g and the two out-of-plane A_g vibrational modes.[16,18,19] Comparing the energy–dispersive X–ray (EDX) spectrum of the $ReSe_2$ nanosheet on$Si/SiO_2$with the EDX spectrum of the substrate further confirms the chemical composition of the flake. Actually, the blue spectrum exhibits a Se peak and a Re peak; the latter is enveloped in the Si peak, returning a shoulder (Figure 1d).

© 2023 The Authors. Advanced Electronic Materials published by Wiley-VCH GmbH

2199160x, 0, Downloaded from https://onlinelibrary.wiley.com/doi/10.1002/aelm.202300066 by CochraneItalia, Wiley Online Library on [14/06/2023]. See the Terms and Conditions (https://onlinelibrary.wiley.com/terms-and-conditions) on Wiley Online Library for rules of use; OA articles are governed by the applicable Creative Commons License

2199160x, 0, Downloaded from https://onlinelibrary.wiley.com/doi/10.1002/aelm.202300066 by CochraneItalia, Wiley Online Library on [14/06/2023]. See the Terms and Conditions (https://onlinelibrary.wiley.com/terms-and-conditions) on Wiley Online Library for rules of use; OA articles are governed by the applicable Creative Commons License

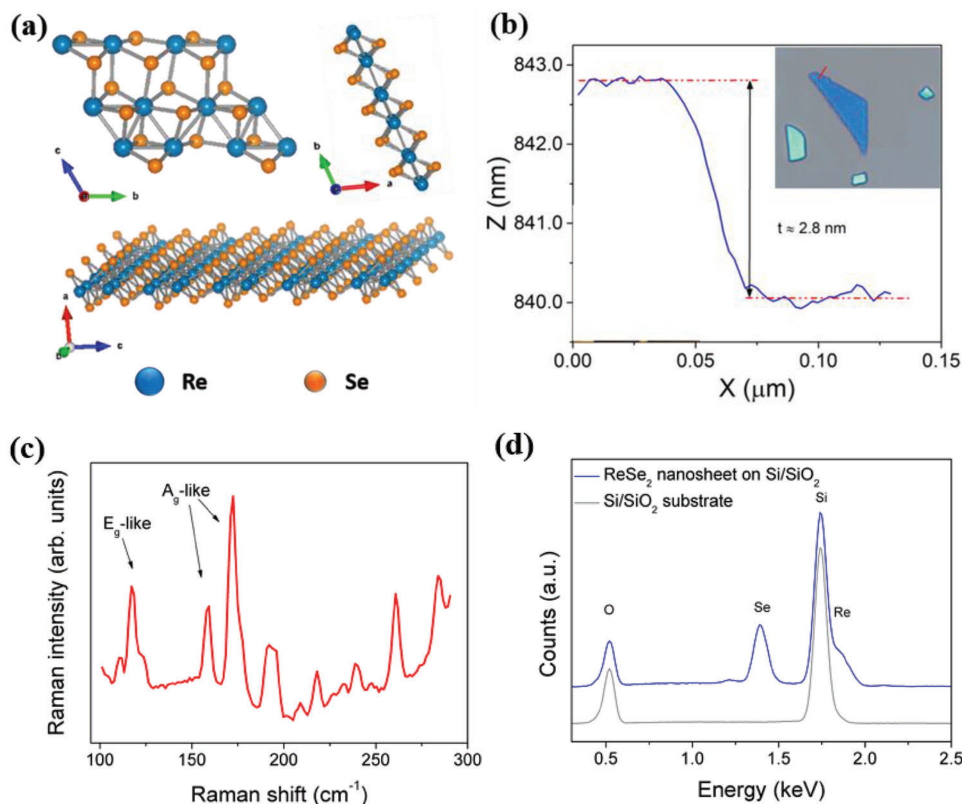

Figure 1. a) Top view and side view along the a,b and c axes of $ReSe_2$ atomic structure: the blue and orange spheres represent Re and Se atoms, respectively. b) AFM step height scan acquired on the highlighted red trace on the $ReSe_2$ flake shown in the microscope image inset. c) Raman spectrum of $ReSe_2$ on SiO_2/Si substrate. d) EDX spectrum of $ReSe_2$ on Si/SiO_2 compared with the EDX spectrum of the Si/SiO_2 substrate.

2.2. Electrical Measurements

Electrical measurements were carried out on the $ReSe_2$ flake exfoliated onto heavily doped Si/SiO_2 (300 nm), which serves as a back-gate for the field effect transistor with source-drain contacts consisting of Cr/Au (5 /50 nm) metal leads fabricated using standard electron beam lithography, thermal deposition, and lift-off technique (**Figure 2**a). The measurement setup shows that the source is grounded, the drain bias is applied to the opposite metal lead, and the gate voltage is applied to the Si substrate. A top view of the device is provided by the SEM image in Figure 2b showing the triangular shape of the flake and the interdigitated design of the metal contacts, corresponding to a total channel width of W = 4.25 μm and a length of L = 0.65 μm. The interdigitated pattern, indeed, makes the device have five parallel channels of equal length and variable width. L is measured as the distance between the metallic leads, while W is the sum of the average widths of the five parallel channels.

The $ReSe_2$ transistor was initially characterized in the dark and at room pressure and temperature. Figure 2c shows the output characteristics of the device, that is, the measured drain current (I_d) as a function of the source-drain voltage bias (V_{ds}) for fixed values of the back gate voltage (V_{gs}). Whereas a representative transfer curve obtained by measuring I_d as a function of V_{gs} for fixed V_{ds} is shown in Figure 2d. The output curves show that both the drain and gate voltages modulate the drain current. The slight asymmetry in the two branches of the output curves for positive and negative drain voltages, together with the limited on-current at V_{gs} = 30 V are indicative of low Schottky barriers at the $ReSe_2$/CrAu interfaces.[31,32] A narrow hysteresis is visible between the forward and reverse sweeps. However, it is not as wide as reported in other works, where it has been associated with the selenium vacancy migration at grain boundaries.[33,34] As I_d is suppressed for negative gate biases, $ReSe_2$ exhibits n-type conduction. The pristine monolayer $ReSe_2$ FETs were previously reported to exhibit p-type behavior,[35] while bulk $ReSe_2$ FETs exfoliated with the modified Bridgman method showed n-type behavior. In fact, the crystal growth of $ReSe_2$ is very challenging, and the adoption of a specific halogen vapor transport route can lead to unintentional background doping.[16] The transfer curve confirms that the $ReSe_2$ device has a dominant n-type behavior, as it turns on at positive gate voltages. In detail, the threshold voltage is $\approx V_{gs}$ = 20 V. However, hole-type conduction occurs for negative V_{gs}. Ambipolar charge transport is observed when the Fermi level of the metal contact is in the middle of the band gap of the channel material and the Fermi level of the channel material itself is near the middle of its band gap. The bandgap of the multilayer $ReSe_2$ has been reported to be ≈1.0 eV with the conduction band minimum and valence band maximum calculated to be 4.55 and 5.65 eV, respectively. Kelvin probe force microscopy, performed on chemical vapor deposition-grown $ReSe_2$ FET with Au contacts, confirmed a $ReSe_2$ work function of 5.0 eV, close to the

© 2023 The Authors. Advanced Electronic Materials published by Wiley-VCH GmbH

2199160x, 0, Downloaded from https://onlinelibrary.wiley.com/doi/10.1002/aelm.202300066 by CochraneItalia, Wiley Online Library on [14/06/2023]. See the Terms and Conditions (https://onlinelibrary.wiley.com/terms-and-conditions) on Wiley Online Library for rules of use; OA articles are governed by the applicable Creative Commons License

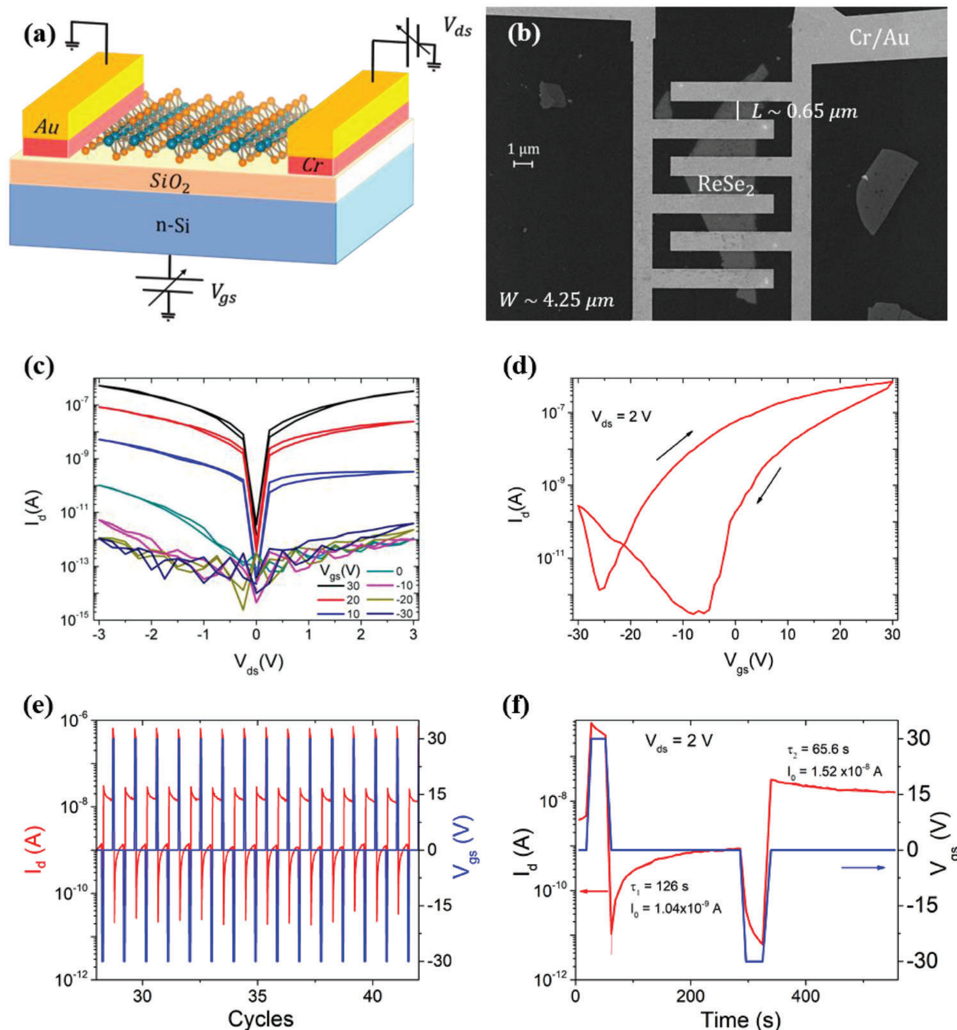

Figure 2. a) Schematic of the device structure and the measurements set up: The $ReSe_2$ flake is deposited onto a SiO_2/Si substrate acting as a global back gate, and the metal contacts are Cr/Au bilayers. The source is grounded, while drain and gate voltages are stepped or swept as needed. b) Scanning electron microscope (SEM) image of the $ReSe_2$ back-gated FET with interdigitated source/drain leads. c) Output curves were measured by sweeping the drain voltage in the (−3, 3) V range, while the gate voltage was sampled in the (−30, 30) V range with steps of 10 V. d) Transfer curve, obtained by forward and reverse sweeps of the gate bias in (-30, 30) V range, at a fixed $V_{ds} = 2$ V. The measurements in (c),(d) were performed in dark and at ambient pressure and temperature. e) Repeated set-read-reset-read cycles: The drain current (red line) is recorded for $V_{gs} = \pm 30$ V pulses or at $V_{gs} = 0$ V (blue line). The current is stable after 30 cycles. f) A single reset-read-set-read cycle showing the two stable current levels corresponding to the “0” and “1” memory bits that are reached after the exponential increase/decline characterized by the reported time constants.

work function of Au, thus accounting for the observed symmetric ambipolar behavior.[24,36] In the device under study, Cr contacts, with a work function around 4.5 eV, favor electron injection. The transfer curve is used to extract the field effect mobility, which was estimated as $\mu = 0.54$ cm^2 V^{-1} s^{-1} by using the equation:

$$\mu = \frac{L}{W}\frac{1}{C_{ox}V_{ds}}\frac{dI_d}{dV_{gs}} \tag{1}$$

where $C_{ox} = 1.15 \times 10^{-8}$ F cm^{-2} is the gate dielectric capacitance per unit area. This is higher than previously reported values for three- or four-layer exfoliated $ReSe_2$ flakes with Cr/Au metal contacts.[23,33] However, compared to other popular 2D metal dichalcogenides, such as MoS_2, $PdSe_2$, $PtSe_2$, or BP the mobility is modest.[37–43] The low mobility can be explained by considering the Schottky barriers and trap levels due to intrinsic defects, adsorbates on the surface, and extrinsic traps at the $ReSe_2/SiO_2$ interface.[44–46] The high subthreshold swing SS = 1.1 V $decade^{-1}$, although lower than previously reported,[23,33] supports the idea of a relatively high defect density at the interface with the SiO_2 layer. Conventionally, Si and SiO_2 have, indeed, considerable surface defects and maintain highly active charge-trapping capacities.[47] The presence of trap states is further confirmed by the occurrence of hysteresis in the transfer curve. Hysteresis is the result of a shift in the transfer characteristic for consecutive forward/reverse gate voltage sweeps and is attributed to charge trapping inside the channel material, interface trap states, and surface-adsorbate-induced traps.[48–51] The left shift

© 2023 The Authors. Advanced Electronic Materials published by Wiley-VCH GmbH

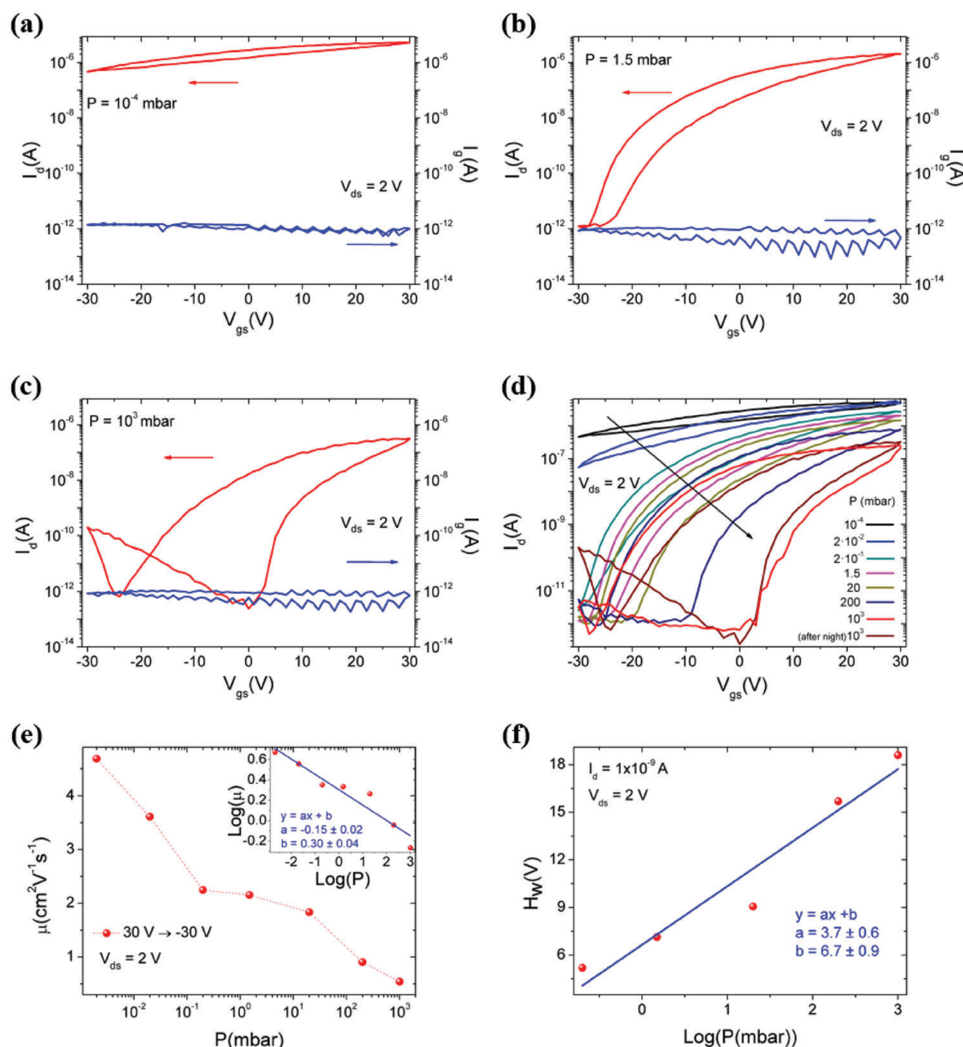

Figure 3. I_d versus V_{gs} (red) and I_{gs} versus V_{gs} (blue) at a) 10^{-4} mbar, b) 1.5 mbar, and c) ambient pressure. d) Dynamical evolution of transfer curves from 10^{-4} mbar to ambient pressure. e) Maximum mobility as a function of pressure. The log-log plot in the inset indicates that mobility follows a power law of pressure (blue line is a linear fit). f) Hysteresis width, computed at the fixed current $I_d = 1$ nA, versus Log(P). Linear fit is reported as a blue line.

of the transfer curve after a reverse voltage sweep corresponds to trapped positive charges. Since it makes transistors' outcomes dependent on the biasing history, hysteresis is undesirable, but it can be exploited to fabricate memory devices. Figures 2e,f show multiple and single set-read-reset-read cycles, obtained over a series of $V_{gs} = \pm 30$ V pulses, which lasted 45 s each, interspersed with $V_{gs} = 0$ V reading cycles, set for 220 s. The rise and fall times of the bias signal were computed by taking into account the average temporal distance between 10% and 90% of the rising and falling signal edges. In detail, the rise and fall times for the $V_{gs} = 30$ V pulses are ≈8.3 and 8.1 s, respectively, while for $V_{gs} = -30$ V they are 8.2 and 5.3 s, respectively. The highest and lowest voltage pulses act as reset and set, making the drain current increase and decrease rapidly: The device is set on the lower/higher branch of the transfer curve by the $V_{gs} = 30$ (−30) V pulse. The two stable current levels obtained for $V_{gs} = 0$ V, after a transient developing over the time scales indicated in Figure 2f, define the two memory states, i.e., the two bits. After ≈30 cycles (see Figure 2e), the memory window, which is the separation between the two current levels, is constant. It is about one order of magnitude wide.

2.3. Effect of Pressure

Electrical measurements were also carried out at different pressures. **Figure 3**a,b,c, show the drain current and gate current versus gate voltage, at increasing pressures, namely 10^{-4}, 1.5 mbar, and ambient pressure. The gate current was monitored to ensure that there is no leakage through the oxide. Remarkably, as summarized in Figure 3d, the conductivity decreases and the hysteresis widens with increasing pressure, i.e., when the adsorption rate of air molecules on the $ReSe_2$ surface increases. Indeed, when the device is exposed to air, molecules such as H_2O and O_2 are adsorbed on the channel surface. H_2O molecules are generally physisorbed on 2D materials, while O_2 can also be chemisorbed when the corresponding energy barrier is

 © 2023 The Authors. Advanced Electronic Materials published by Wiley-VCH GmbH

2199160x, 0, Downloaded from https://onlinelibrary.wiley.com/doi/10.1002/aelm.202300066 by CochraneItalia, Wiley Online Library on [14/06/2023]. See the Terms and Conditions (https://onlinelibrary.wiley.com/terms-and-conditions) on Wiley Online Library for rules of use; OA articles are governed by the applicable Creative Commons License

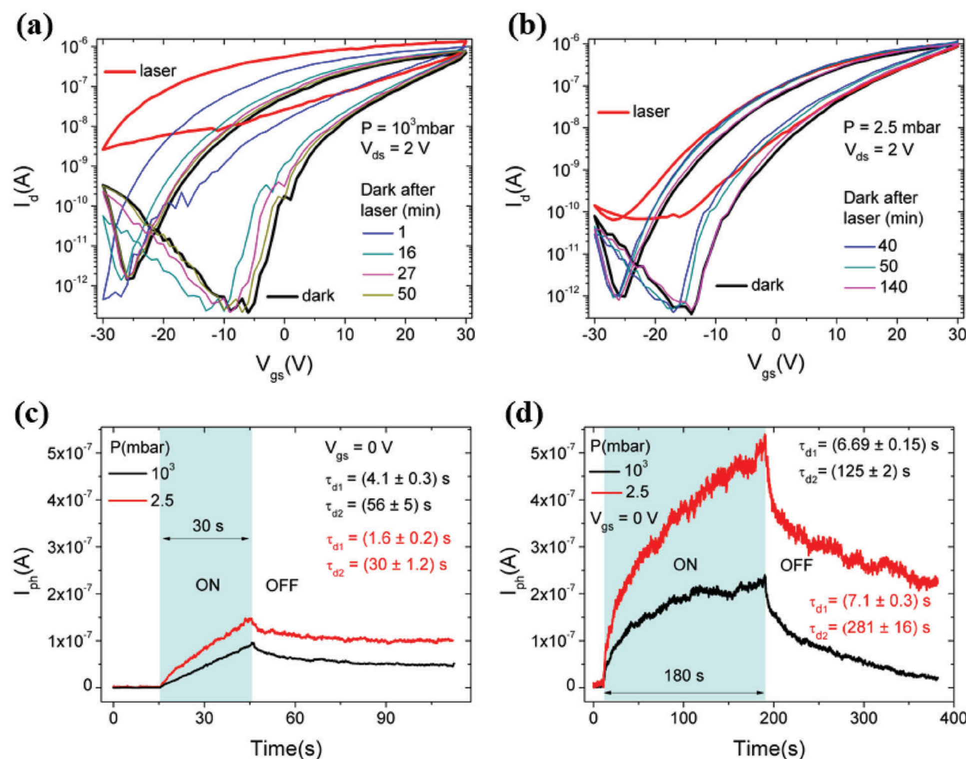

Figure 4. Transfer curves measured in the dark (black) and under laser illumination (red) at ambient pressure a) and low vacuum b). The thinner lines correspond to measurements recorded with increasing delays after the laser was switched off. Photo response to c) 30 and d) 180 s long laser pulses (light-blue shadow), at V_{gs} = 0 V and at different pressures. The current after each pulse is fitted by two exponential decays and the time constants are reported.

overcome.[52] First–principles calculations on single-layer $ReSe_2$ nanosheets yield low adsorption energy of −162 meV for O_2 molecules,[35] which means that O_2 is only physisorbed and can be easily removed by reducing the pressure. H_2O and O_2, being electronegative, act as acceptors, therefore, they cause a reduction of the carrier concentration when they are adsorbed on the surface of the channel. By lowering pressure, the conductivity increases because of the air molecules' desorption, which releases electrons into the channel. The n-type doping of the device increases, and the Fermi level moves toward the conduction band. However, the increased doping makes the transfer curve shift to the left, and the device does not switch off, making the ambipolar behavior unobservable. As expected, the p-type conduction in the transfer curve is restored when pressure is increased again, as shown in Figure 3d.

Figure 3d depicts the dynamical evolution of transfer curves as pressure is raised from high vacuum to ambient pressure. These curves are used to find the dependence of some FET parameters on pressure. Field effect mobility, extracted from the reverse branches with V_{gs} from 30 to -30 V, decreases with increasing pressure because the adsorbed molecules act as scattering centers. The log-log plot in the inset of Figure 3e confirms that the mobility follows a power law of the pressure.[33] Adsorbate-induced trap states also account for a wider hysteresis at ambient pressure. The hysteresis width H_w, defined as the difference of the gate voltages at a current of 1 nA, linearly decreases as a function of pressure on a semi-log scale (Figure 3f).

2.4. Photoresponse

The photoresponse of the device exposed to the light of a supercontinuum white laser was investigated as a function of the pressure. At ambient pressure, see **Figure 4**a, positive photoconductivity (PPC) occurs. Indeed, the drain current under laser illumination is higher than in dark conditions for both transfer branches, at each gate voltage. The difference between the two curves gets more pronounced for negative gate voltages; moreover, the transistor does not switch off when illuminated. Figure 4b shows that PPC is still present in a low vacuum. To check if the phenomenon is reversible, the time evolution of the curves was studied. A time of ≈145 min is needed in a vacuum to restore the pre-illumination state, but relaxation occurs faster in air, with a time of ≈50 min.

To gain more insights into the photoresponse behavior, the device at V_{gs} = 0 V was exposed to 30 and 180 s laser pulses at 100% power. In Figures 4c,d, I_{ph} stands for the difference between the current under illumination and the current in darkness (I_{ph} = I_{light}-I_{dark}). The dark levels are different for the two pressures but have been purposely shifted to zero for comparison.

Figure 4c shows linearly increasing photocurrents, both at ambient pressure and at 2.5 mbar, pointing out that 30 s of laser illumination are not enough to achieve the maximum photocurrent. The decay after the laser switches off is slow, and the photocurrent does not return to the dark level after a time of 100 s (persistent photoconductivity). The photocurrent behavior under 180 s

© 2023 The Authors. Advanced Electronic Materials published by Wiley-VCH GmbH

2199160x, 0, Downloaded from https://onlinelibrary.wiley.com/doi/10.1002/aelm.202300066 by CochraneItalia, Wiley Online Library on [14/06/2023]. See the Terms and Conditions (https://onlinelibrary.wiley.com/terms-and-conditions) on Wiley Online Library for rules of use; OA articles are governed by the applicable Creative Commons License

ADVANCED ELECTRONIC MATERIALS Open Access
www.advelectronicmat.de

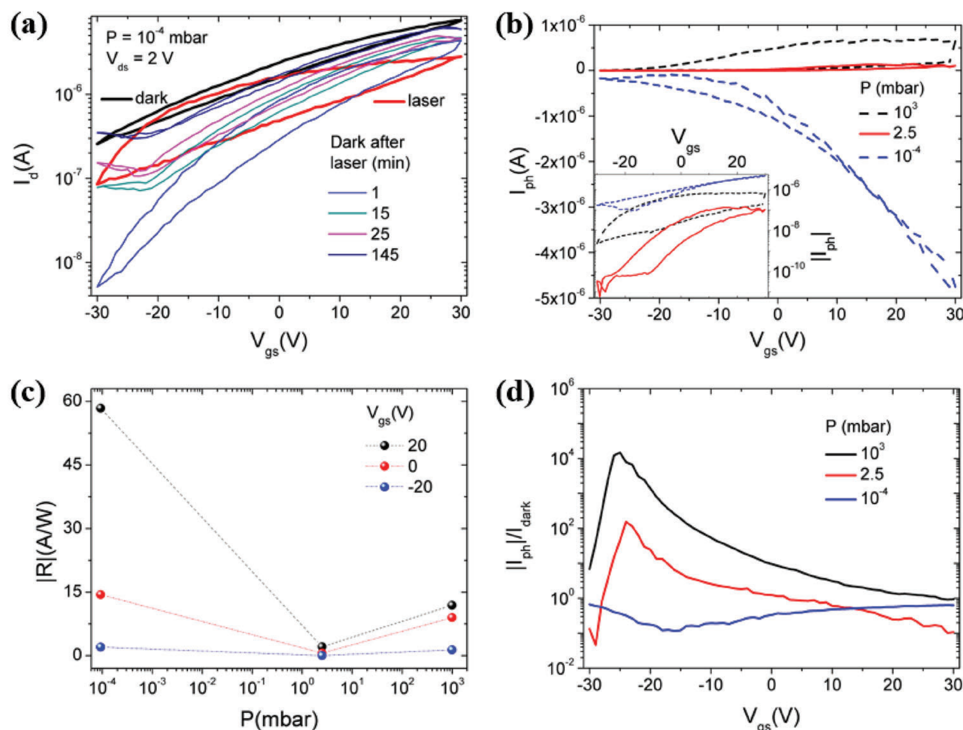

Figure 5. a) Transfer curves obtained at 10^{-4} mbar in dark (black) and under laser illumination (red). The thinner colored lines were recorded at different times after the laser was turned off. b) Photocurrent ($I_{ph} = I_{light}$-I_{dark}) as a function of the gate voltages at three different pressures: 10^3 mbar (black line), 2.5 mbar (red line), and 10^{-4} mbar (blue line). The inset compares the absolute values of the photocurrent at different pressures. c) Photoresponsivity as a function of pressure, extracted at $V_{gs} = 20$ V (black spheres), 0 V (red spheres), and -20 V (blue spheres). d) Photocurrent normalized to the dark current level (I_{ph}/I_{dark}) as a function of gate voltages at different pressures.

laser pulses reveals that both the rise and the decay are double-exponential processes with shorter (<10 s) and longer (>100 s) time constants, obtained by fitting the curve

$$y = Ae^{-\frac{t}{\tau_1}} + Be^{-\frac{t}{\tau_2}} + y_0 \tag{2}$$

Generally, the shorter decay component is attributed to photocarrier recombination and trapping in shallower traps, while the longer one is due to photogating effects caused by deeper traps and adsorbates.[53,54]

The slow rise of the photocurrent can be attributed to laser-assisted desorption of adsorbates,[54,55] a slow process that can account for the positive photoconductivity and overcome the electron-hole photogeneration and trapped carrier photoexcitation processes. As reported above, H_2O and O_2 molecules can easily be adsorbed on the surface, but, since they are only physisorbed, the energy transferred by the laser is sufficient to enable their removal from the surface. Therefore, light can have an effect similar to that of lowering pressure because it promotes electron transfer from desorbed air molecules to the channel, which increases the electron density and the conductivity of $ReSe_2$. As a result, the shorter time constants can be linked to the generation/recombination process of photogenerated or photoexcited carriers, while the longer response is ascribed to the slow adsorption/desorption of the air molecules on the channel surface.[55] This conclusion is supported by the fact that a shorter relaxation time is observed at ambient pressure (see Figure 4d), which facilitates the desorption and adsorption processes. This is consistent with the observation that p-type conduction is suppressed more at ambient pressure than in a vacuum. Actually, light is able to reduce the ambipolar behavior because both photogeneration and molecule desorption increase the electron concentration, so that the Fermi level moves away from the middle of the gap, as already explained in Section 2.2. The same result can be expected at a higher temperature, which will facilitate the desorption of adsorbates.

The transfer curves in a higher vacuum, 10^{-4} mbar, in **Figure 5**a reveal that, when the device is illuminated, the drain current is lower than it was in the dark, i.e., there is a negative photoconductivity (NPC). NPC has been reported in various inorganic, organic, and organic–inorganic hybrid materials, but its origin is still under debate. It was attributed to the photogating of the majority carriers in InAs and Cd_3As_2 nanowires[56,57] and to the photoassisted oxygen desorption in p-type low dimensional photodetectors (LDPD) with bare materials.[39,58] In this case, NPC can be ascribed to the trapping mechanisms of electrons by defect-induced trap states, such as Se vacancies-induced states, localized both in the material and at the interface with the oxide. When the laser is turned on, some of the electrons are excited from the valence band to the upper impurity levels.[59] Interface trap states above the intrinsic Fermi level, when filled, expose a negative charge and generate a negative built-in potential that enables a right-shift of the transfer curve with a reduction in conductivity. The photoinduced local gate voltage has a relationship

© 2023 The Authors. Advanced Electronic Materials published by Wiley-VCH GmbH

2199160x, 0, Downloaded from https://onlinelibrary.wiley.com/doi/10.1002/aelm.202300066 by CochraneItalia, Wiley Online Library on [14/06/2023]. See the Terms and Conditions (https://onlinelibrary.wiley.com/terms-and-conditions) on Wiley Online Library for rules of use; OA articles are governed by the applicable Creative Commons License

with the applied gate voltage.[60] In fact, the interface trap states are gradually filled by electrons with the rise of the Fermi level, i.e., by applying positive gate voltages. This mechanism leaves the corresponding photogenerated holes to recombine with the free electrons in the channel so that both processes contribute to lowering the carrier concentration. After the light is switched off, the carrier photogeneration ends and the electrons are gradually detrapped. However, soon after switching off the laser, some electrons are not yet released and might originate a dark current lower than the initial one.[56] This can be observed in the behavior of the transfer characteristic measured after 1 min of switching off.

This mechanism is partially suppressed at ambient pressure because Se vacancies are already healed by oxygen atom substitutions, so the gap states induced by vacancies in Se sites are quenched by isoelectronic substitutions. In $ReSe_2$ monolayer, in fact, only a small energy barrier (of ≈84 meV) needs to be overcome to allow external O_2 molecules to dissociate when an O_2 molecule is adsorbed at Se vacancies so that they are subsequently filled by dissociated O atoms.[61] Therefore, when the laser is switched on at ambient pressure, most traps are already filled, and, as discussed above, the dominant mechanism becomes the photo-assisted desorption of the electronegative molecules, which returns PPC. At an intermediate pressure, both phenomena impact the photocurrent. Since they are competitive mechanisms leading to opposite-polarity photoresponses, their combination results in a low photocurrent.

Figure 5b compares the photocurrent at different pressures. The highest $|I_{ph}| = |I_{light}\text{-}I_{dark}|$ is reached in high vacuum for each gate voltage, while the lowest is obtained in low vacuum for the reasons above.

To further investigate $ReSe_2$ optical properties, the photoresponsivity,

$$R = \left| I_{ph}/PS \right| \tag{3}$$

where P is the laser intensity and S is the effective illuminated area of the device, was computed at different pressures and for different gate voltages and reported in Figure 5c. At each pressure, the highest photoresponsivity is achieved at $V_{gs} = +20$ V.

However, to evaluate the performance of photodetectors, the dark current level is crucial. Thus, the I_{ph}/I_{dark} ratio is reported in Figure 5d. At a pressure of 10^{-4} mbar, this ratio is lower than in ambient conditions for the whole voltage gate range. Similarly, the observed I_{ph}/I_{dark} ratio is higher at ambient pressure than in low vacuum, because the drain current in darkness and in low vacuum is of the same order of magnitude as at ambient pressure, while the photocurrent is about one order of magnitude lower. Such an observation suggests that the impact of light is more effective at ambient pressure. Moreover, at ambient pressure and at 2.5 mbar, the curves have a peaked profile that is due to the ambipolar characteristics of the dark current, which indicates that the best signal-to-noise ratio is achieved at the transition between p- and n-type conditions, i.e., at $V_{gs} \approx -25$ V.

It is worth noting that the in-plane anisotropic structure of $ReSe_2$ crystals can affect their optical properties. Polarized incident light is absorbed in different ways depending on its alignment with respect to crystal directions. It has been found that the photocurrent is maximum for incident light polarized along the b-axis and minimum in the perpendicular direction.[20] Having control over the polarization of the light could enable the device to have the highest photocurrent. However, the polarization of light is not expected to have an impact on the main photoresponse mechanisms considered in this work, which was conducted using a non-polarized laser. Moreover, the $ReSe_2$ flake used in the device under study might contain grains with various orientations that could average the effects of anisotropy.

3. Conclusion

We have reported and discussed the electro-optical features of a back–gated field effect transistor with a few-layer $ReSe_2$ channel and Cr/Au metal contacts. The device exhibits dominant n-type conduction and a wide hysteresis in the transfer characteristic, which has been exploited for memory applications. We have demonstrated that air pressure strongly affects the performance of the device, whose conductivity and mobility are higher in high vacuum, due to the reduced density of adsorbates. We investigated the photoresponse, showing that it undergoes a transition from PPC at ambient pressure to NPC at 10^{-4} mbar, which we explained considering the interplay between photo-assisted air molecules desorption and photogenerated electron trapping. The dynamical evolution of the photocurrent under a laser pulse showed a double-exponential decay in which adsorbates can play a crucial role. We finally showed that the highest photocurrent to dark current ratio is achieved at ambient pressure and at the gate voltage separating the p- and n-type conduction. Our study unveiled several properties of 2D $ReSe_2$ through a comprehensive investigation of conductivity and photoconductivity as a function of air pressure.

4. Experimental Section

A standard mechanical exfoliation technique was applied to produce ultrathin $ReSe_2$ flakes from bulk $ReSe_2$ single crystals. The flakes were transferred onto highly doped n-type silicon substrates, previously covered by 290 nm-thick SiO_2, which acts as a global back gate. Metal contacts were defined using photolithography and the traditional lift-off process of evaporated Cr/Au (5/100 nm).

Devices were placed in a Janis ST-500 Probe Station (Lake Shore Cryotronics, Inc.) equipped with nanoprobes connected to the source/drain leads. Measurements were carried out in a two-probe configuration. The sample holder of the probe station, which was in direct electrical contact with the Ag–pasted n-Si substrate, was used to apply the back-gate voltage. The measurements were performed by the source-measurement units of a semiconductor characterization system Keithley 4200 SCS.

For the transistor characterization, the source was grounded, while drain and gate voltages were either swept or stepped according to the current–voltage (IV) test performed, and the drain and gate currents were monitored.

Transfer characteristics were obtained by fixing the drain voltage at 2 V and sweeping the gate voltage from -30 to 30 V in a quiet mode with a sweep delay of 0.2 s. Similarly, output characteristics were obtained by sweeping the drain voltage from -3 to 3 V, while the gate bias was varied at steps of 10 V in the interval (-30; 30) V. For both the curves, a double sweep, forward, and reverse, was adopted.

The electric measurements were carried out at controlled pressure, from ambient pressure to $\approx 10^{-4}$ mbar, through a series of rotatory and

© 2023 The Authors. Advanced Electronic Materials published by Wiley-VCH GmbH

2199160x, 0, Downloaded from https://onlinelibrary.wiley.com/doi/10.1002/aelm.202300066 by CochraneItalia, Wiley Online Library on [14/06/2023]. See the Terms and Conditions (https://onlinelibrary.wiley.com/terms-and-conditions) on Wiley Online Library for rules of use; OA articles are governed by the applicable Creative Commons License

turbomolecular pumps. The pressure was monitored by the pressure gauge TPG261.

A supercontinuum white laser source with an intensity of 20 mW mm^{-2} and a wavelength in the 450–2500 nm range was used to investigate the photoresponse of the device.

Finally, a Raman Spectrometer (RENISHAW InVia), in backscattering geometry, was used to extract the vibrational properties of the investigated device. A near–infrared laser with a wavelength of 785 nm, was employed as the excitation source, and the spectra were acquired in the range 100–300 cm^{-1} with 100× magnification, 10 s exposure time, 10% laser power, and 5 accumulations.

The height profile of the $ReSe_2$ flakes was measured by atomic force microscopy (NaioAFM by Nanosurf AG).

Acknowledgements

A.D.B. acknowledges the financial support by University of Salerno, grant ORSA223384. MFC and SR acknowledge financial support by EPSRC (EP/V048163/1, EP/V052306/1) and the Leverhulme Trust. The authors thank Pietro Campiglia and Carlo Crescenzi for the use of Raman microscope at University of Salerno.

Conflict of Interest

The authors declare no conflict of interest.

Data Availability Statement

The data that support the findings of this study are available from the corresponding author upon reasonable request.

Keywords

field effect transistors, memories, negative photoconductivity, photodetectors, rhenium diselenide

Received: February 9, 2023
Revised: April 28, 2023
Published online:

[1] S. Manzeli, D. Ovchinnikov, D. Pasquier, O. V. Yazyev, A. Kis, *Nat. Rev. Mater.* **2017**, *2*, 17033.
[2] A. Di Bartolomeo, *Nanomaterials* **2020**, *10*, 579.
[3] T. Chowdhury, E. C. Sadler, T. J. Kempa, *Chem. Rev.* **2020**, *120*, 12563.
[4] S. Tajik, Z. Dourandish, F. Garkani Nejad, H. Beitollahi, P. M. Jahani, A. Di Bartolomeo, *Biosens. Bioelectron.* **2022**, *216*, 114674.
[5] N. Goel, M. Kumar, *Nano Express* **2021**, *2*, 031001.
[6] S. Das, A. Sebastian, E. Pop, C. J. McClellan, A. D. Franklin, T. Grasser, T. Knobloch, Y. Illarionov, A. V. Penumatcha, J. Appenzeller, Z. Chen, W. Zhu, I. Asselberghs, L.-J. Li, U. E. Avci, N. Bhat, T. D. Anthopoulos, R. Singh, *Nat. Electron.* **2021**, *4*, 786.
[7] A. Di Bartolomeo, *Nanomaterials* **2022**, *12*, 2125.
[8] B. Rawat, V. M. M, R. Paily, *IEEE Trans. Electron Devices* **2019**, *66*, 2424.
[9] O. Lopez-Sanchez, D. Lembke, M. Kayci, A. Radenovic, A. Kis, *Nat. Nanotechnol.* **2013**, *8*, 497.
[10] W. Choi, M. Y. Cho, A. Konar, J. H. Lee, G. B. Cha, S. C. Hong, S. Kim, J. Kim, D. Jena, J. Joo, S. Kim, *Adv. Mater.* **2012**, *24*, 5832.
[11] N. Perea-López, A. L. Elías, A. Berkdemir, A. Castro-Beltran, H. R. Gutiérrez, S. Feng, R. Lv, T. Hayashi, F. López-Urías, S. Ghosh, B. Muchharla, S. Talapatra, H. Terrones, M. Terrones, *Adv. Funct. Mater.* **2013**, *23*, 5511.
[12] A. Arora, J. Noky, M. Drüppel, B. Jariwala, T. Deilmann, R. Schneider, R. Schmidt, O. Del Pozo-Zamudio, T. Stiehm, A. Bhattacharya, P. Krüger, S. Michaelis de Vasconcellos, M. Rohlfing, R. Bratschitsch, *Nano Lett.* **2017**, *17*, 3202.
[13] S. Lee, R. Peng, C. Wu, M. Li, *Nat. Commun.* **2022**, *13*, 1485.
[14] V. O. Yukhymchuk, L. Kulikov, M. Valakh, A. Litvinchuk, M. Skoryk, N. Mazur, V. Yefanov, O. Selyshchev, V. Dzhagan, D. Zahn, *J. Raman Spectrosc.* **2020**, *51*, 1305.
[15] B. Jariwala, A. Thamizhavel, A. Bhattacharya, *J. Phys. D: Appl. Phys.* **2017**, *50*, 044001.
[16] B. Jariwala, D. Voiry, A. Jindal, B. A. Chalke, R. Bapat, A. Thamizhavel, M. Chhowalla, M. Deshmukh, A. Bhattacharya, *Chem. Mater.* **2016**, *28*, 3352.
[17] L. S. Hart, J. L. Webb, S. Dale, S. J. Bending, M. Mucha-Kruczynski, D. Wolverson, C. Chen, J. Avila, M. C. Asensio, *Sci. Rep.* **2017**, *7*, 5145.
[18] D. Wolverson, S. Crampin, A. S. Kazemi, A. Ilie, S. J. Bending, *ACS Nano* **2014**, *8*, 11154.
[19] Ł. Kipczak, M. Grzeszczyk, K. Olkowska-Pucko, A. Babiński, M. R. Molas, *J. Appl. Phys.* **2020**, *128*, 044302.
[20] E. Zhang, P. Wang, Z. Li, H. Wang, C. Song, C. Huang, Z.-G. Chen, L. Yang, K. Zhang, S. Lu, W. Wang, S. Liu, H. Fang, X. Zhou, H. Yan, J. Zou, X. Wan, P. Zhou, W. Hu, F. Xiu, *ACS Nano* **2016**, *10*, 8067.
[21] B. Silva, J. Rodrigues, B. Sompalle, C.-D. Liao, N. Nicoara, J. Borme, F. Cerqueira, M. Claro, S. Sadewasser, P. Alpuim, A. Capasso, *Nanomaterials* **2021**, *11*, 1650.
[22] C. M. Corbet, S. S. Sonde, E. Tutuc, S. K. Banerjee, *Appl. Phys. Lett.* **2016**, *108*, 162104.
[23] N. R. Pradhan, C. Garcia, B. Isenberg, D. Rhodes, S. Feng, S. Memaran, Y. Xin, A. McCreary, A. R. H. Walker, A. Raeliarijaona, H. Terrones, M. Terrones, S. McGill, L. Balicas, *Sci. Rep.* **2018**, *8*, 12745.
[24] B. Kang, Y. Kim, J. H. Cho, C. Lee, *2D Mater.* **2017**, *4*, 025014.
[25] K. Lee, S. Yang, Y. Sung, Y. Chang, C. Lin, F. Yang, M. Li, K. Watanabe, T. Taniguchi, C.-H. Ho, C. Lien, Y.-F. Lin, *Adv. Funct. Mater.* **2019**, *29*, 1809011.
[26] S.-H. Jo, H. W. Lee, J. Shim, K. Heo, M. Kim, Y. J. Song, J.-H. Park, *Adv. Sci.* **2018**, *5*, 1700423.
[27] M. F. Khan, S. Rehman, I. Akhtar, S. Aftab, H. M. S. Ajmal, W. Khan, D. Kim, J. Eom, *2D Mater.* **2019**, *7*, 015010.
[28] M. H. Ali, D.-H. Kang, J.-H. Park, *Org. Electron.* **2018**, *53*, 14.
[29] Y. Huang, Y. Gu, X. Wu, R. Ge, Y.-F. Chang, X. Wang, J. Zhang, D. Akinwande, J. C. Lee, *Front. Nanotechnol.* **2021**, *3*, 782836.
[30] G. Nazir, A. Rehman, S. Hussain, O. Hakami, K. Heo, M. A. Amin, M. Ikram, S. A. Patil, M. A. U. Din, *Nanomaterials* **2022**, *12*, 3713.
[31] A. Di Bartolomeo, A. Grillo, F. Urban, L. Iemmo, F. Giubileo, G. Luongo, G. Amato, L. Croin, L. Sun, S.-J. Liang, L. K. Ang, *Adv. Funct. Mater.* **2018**, *28*, 1800657.
[32] A. Grillo, A. Di Bartolomeo, *Adv. Electron. Mater.* **2021**, *7*, 2000979.
[33] E. Faella, K. Intonti, L. Viscardi, F. Giubileo, A. Kumar, H. T. Lam, K. Anastasiou, M. F. Craciun, S. Russo, A. Di Bartolomeo, *Nanomaterials* **2022**, *12*, 1886.
[34] V. K. Sangwan, D. Jariwala, I. S. Kim, K.-S. Chen, T. J. Marks, L. J. Lauhon, M. C. Hersam, *Nat. Nanotechnol.* **2015**, *10*, 403.
[35] S. Yang, S. Tongay, Y. Li, Q. Yue, J.-B. Xia, S.-S. Li, J. Li, S.-H. Wei, *Nanoscale* **2014**, *6*, 7226.
[36] J. Kim, K. Heo, D.-H. Kang, C. Shin, S. Lee, H.-Y. Yu, J.-H. Park, *Adv. Sci.* **2019**, *6*, 1901255.
[37] A. Pelella, A. Grillo, F. Urban, F. Giubileo, M. Passacantando, E. Pollmann, S. Sleziona, M. Schleberger, A. Di Bartolomeo, *Adv. Electron. Mater.* **2021**, *7*, 2000838.
[38] F. Urban, F. Gity, P. K. Hurley, N. McEvoy, A. Di Bartolomeo, *Appl. Phys. Lett.* **2020**, *117*, 193102.
[39] A. D. Bartolomeo, F. Urban, E. Faella, A. Grillo, A. Pelella, F. Giubileo, M. B. Askari, N. McEvoy, F. Gity, P. K. Hurley, *J. Phys.: Conf. Ser.* **2021**, *1866*, 012001.

© 2023 The Authors. Advanced Electronic Materials published by Wiley-VCH GmbH

2199160x, 0, Downloaded from https://onlinelibrary.wiley.com/doi/10.1002/aelm.202300066 by CochraneItalia, Wiley Online Library on [14/06/2023]. See the Terms and Conditions (https://onlinelibrary.wiley.com/terms-and-conditions) on Wiley Online Library for rules of use; OA articles are governed by the applicable Creative Commons License

[40] P. Ye, H. Xiao, Q. Zhu, Y. Kong, Y. Tang, M. Xu, *Sci. China Mater.* **2022**, *66*, 193.
[41] Q. Feng, F. Yan, W. Luo, K. Wang, *Nanoscale* **2016**, *8*, 2686.
[42] A. Grillo, A. Pelella, E. Faella, F. Giubileo, S. Sleziona, O. Kharsah, M. Schleberger, A. D. Bartolomeo, *2D Mater.* **2021**, *9*, 015028.
[43] A. Di Bartolomeo, A. Pelella, F. Urban, A. Grillo, L. Iemmo, M. Passacantando, X. Liu, F. Giubileo, *Adv. Electron. Mater.* **2020**, *6*, 2000094.
[44] F. Giannazzo, G. Fisichella, A. Piazza, S. Di Franco, G. Greco, S. Agnello, F. Roccaforte, *Beilstein J. Nanotechnol.* **2017**, *8*, 254.
[45] A. Di Bartolomeo, L. Genovese, F. Giubileo, L. Iemmo, G. Luongo, T. Foller, M. Schleberger, *2D Mater.* **2017**, *5*, 015014.
[46] F. Urban, F. Giubileo, A. Grillo, L. Iemmo, G. Luongo, M. Passacantando, T. Foller, L. Madauß, E. Pollmann, M. P. Geller, D. Oing, M. Schleberger, A. Di Bartolomeo, *2D Mater.* **2019**, *6*, 045049.
[47] M. Malik, M. A. Iqbal, J. R. Choi, P. V. Pham, *Front. Chem.* **2022**, *10*, 905404.
[48] F. Urban, F. Giubileo, A. Grillo, L. Iemmo, G. Luongo, M. Passacantando, T. Foller, L. Madauß, E. Pollmann, M. P. Geller, D. Oing, M. Schleberger, A. D. Bartolomeo, *2D Mater.* **2019**, *6*, 045049.
[49] A. Di Bartolomeo, A. Pelella, X. Liu, F. Miao, M. Passacantando, F. Giubileo, A. Grillo, L. Iemmo, F. Urban, S.-J. Liang, *Adv. Funct. Mater.* **2019**, *29*, 1902483.
[50] A. Pelella, O. Kharsah, A. Grillo, F. Urban, M. Passacantando, F. Giubileo, L. Iemmo, S. Sleziona, E. Pollmann, L. Madauß, *ACS Appl. Mater. Interfaces* **2020**, *12*, 40532.
[51] A. Di Bartolomeo, A. Pelella, A. Grillo, F. Urban, F. Giubileo, *Appl. Sci.* **2020**, *10*, 5840.
[52] Y. Liu, P. Stradins, S.-H. Wei, *Angew. Chem., Int. Ed.* **2016**, *55*, 965.
[53] A. D. Bartolomeo, L. Genovese, T. Foller, F. Giubileo, G. Luongo, L. Croin, S.-J. Liang, L. K. Ang, M. Schleberger, *Nanotechnology* **2017**, *28*, 214002.
[54] P. Han, E. R. Adler, Y. Liu, L. St Marie, A. El Fatimy, S. Melis, E. Van Keuren, P. Barbara, *Nanotechnology* **2019**, *30*, 284004.
[55] Y. Wang, Z. He, J. Zhang, H. Liu, X. Lai, B. Liu, Y. Chen, F. Wang, L. Zhang, *Nano Res.* **2020**, *13*, 358.
[56] K. Park, M. Jung, D. Kim, J. R. Bayogan, J. H. Lee, S. J. An, J. Seo, J. Seo, J.-P. Ahn, J. Park, *Nano Lett.* **2020**, *20*, 4939.
[57] N. K. Tailor, C. A. Aranda, M. Saliba, S. Satapathi, *ACS Mater. Lett.* **2022**, *4*, 2298.
[58] A. Grillo, E. Faella, A. Pelella, F. Giubileo, L. Ansari, F. Gity, P. K. Hurley, N. McEvoy, A. Di Bartolomeo, *Adv. Funct. Mater.* **2021**, *31*, 2105722.
[59] C. M. Penchina, J. S. Moore, N. Holonyak, *Phys. Rev.* **1966**, *143*, 634.
[60] H. Fang, W. Hu, *Adv. Sci.* **2017**, *4*, 1700323.
[61] Y. Zhu, L. Tao, X. Chen, Y. Ma, S. Ning, J. Zhou, X. Zhao, M. Bosman, Z. Liu, S. Du, S. T. Pantelides, W. Zhou, *iScience* **2021**, *24*, 103456.

© 2023 The Authors. Advanced Electronic Materials published by Wiley-VCH GmbH

2199160x, 0, Downloaded from https://onlinelibrary.wiley.com/doi/10.1002/aelm.202300066 by CochraneItalia, Wiley Online Library on [14/06/2023]. See the Terms and Conditions (https://onlinelibrary.wiley.com/terms-and-conditions) on Wiley Online Library for rules of use; OA articles are governed by the applicable Creative Commons License